Available online at www.sciencedirect.com
SCIENCE DIRECT®
Journal of Catalysis 221 (2004) 560–574
JOURNAL OF CATALYSIS
www.elsevier.com/locate/jcat

Effect of high-temperature treatment on Fe/ZSM-5 prepared by chemical vapor deposition of $FeCl_3$ I. Physicochemical characterization

E.J.M. Hensen,[a,*] Q. Zhu,[a] M.M.R.M. Hendrix,[b] A.R. Overweg,[c] P.J. Kooyman,[d] M.V. Sychev,[e] and R.A. van Santen [a]

[a] *Schuit Institute of Catalysis, Laboratory of Inorganic Chemistry and Catalysis, Eindhoven University of Technology, PO Box 513, 5600 MB, Eindhoven, The Netherlands*
[b] *Laboratory of Solid State and Materials Chemistry, Eindhoven University of Technology, PO Box 513, 5600 MB Eindhoven, The Netherlands*
[c] *Interfacultair Reactor Institute, Delft University of Technology, Mekelweg 15, 2629 JB, Delft, The Netherlands*
[d] *National Centre for High Resolution Electron Microscopy, Delft University of Technology, Rotterdamseweg 137, 2628 AL Delft, The Netherlands*
[e] *National Technical University of Ukraine, Faculty of Chemical Technology, pr. Peremogy 37, 03056 Kiev, Ukraine*

Received 30 June 2003; revised 19 September 2003; accepted 24 September 2003

Abstract

The effect of severe (hydrothermal) treatment on Fe/ZSM-5 prepared by sublimation of $FeCl_3$ is studied by a combination of high-resolution TEM, EXAFS, ^{57}Fe Mössbauer spectroscopy, IR, UV–vis, nitrogen adsorption, ^{27}Al NMR spectroscopy, and low-temperature nitrous oxide decomposition. The heterogeneous nature of Fe/ZSM-5 is stressed with a preponderance of iron oxide particles on the external zeolite surface. Additionally, neutral iron oxide nanoparticles and charge-compensating iron complexes are located in the micropores. Severe calcination at 973 K induces the growth and ordering of the iron oxide aggregates. Moreover, some of the occluded neutral iron oxide nanoparticles are transformed into charge-compensating iron complexes upon a protolysis reaction with the Brønsted protons. These effects are more pronounced in the case of steaming at 973 K, additionally resulting in the removal of Al from framework positions. Despite the low dispersion of iron oxide in Fe/ZSM-5, relatively low Fe–Fe coordination numbers were derived from the EXAFS data for Fe/ZSM-5; high-temperature treatments increased this number. This low value points to the disordered nature of the iron oxide aggregates rather than to the presence of an abundant fraction of binuclear iron clusters. Titration of sites active in nitrous oxide decomposition shows that their amount increases upon increasing severity of treatment of Fe/ZSM-5. Their number, however, remains very small (a few percent of the total iron) and appears to correlate to the amount of Fe^{2+} present after room temperature exposure to vacuum conditions. A comparison to a commercial HZSM-5 zeolite with a very low iron content is made. The catalytic performance of these materials is discussed in a companion paper (J. Catal. (2003)).

Keywords: Fe/ZSM-5; Sublimation method; Active sites; Nitrous oxide decomposition; Mössbauer spectroscopy; Extended X-ray absorption fine structure; Infrared spectroscopy; Nuclear magnetic resonance

1. Introduction

The limited dimensions of zeolite micropores allow stabilization of small transition metal oxide complexes with unique catalytic properties [1,2]. The redox properties of iron-containing zeolites, most notably with the MFI topology, have attracted widespread attention for a number of potential catalytic applications. Most importantly, such zeolites catalyze the selective insertion of an oxygen atom into the C–H bonds of aromatics and alkanes [3] when nitrous oxide is the oxidant. The particular case of benzene hydroxylation to phenol forms the basis for a potential alternative [4] to the environmentally stressing three-step cumene process. Moreover, these materials may be suitable for abatement of nitrous oxide emissions from nitric acid plants [5–10]. Another potential application field is NO_x reduction for diesel or lean-burn Otto engines, which has resulted in a number of

* Corresponding author.
E-mail address: e.j.m.hensen@tue.nl (E.J.M. Hensen).

0021-9517/$ – see front matter
doi:10.1016/j.jcat.2003.09.024

studies using ammonia (e.g., [11]) or hydrocarbons [12–15] as reductant.

Although there appears to be no general consensus on the nature of the active sites, especially for the activation of nitrous oxide with proposals stressing the importance of Brønsted acid sites [16,17], Lewis acid sites created upon hydrothermal treatment [18–20], and Fe redox sites [21–23] having their share of attention, the latter type of species have been assigned the specific catalytic activity most frequently. It is suggested that the active sites have a dimeric iron structure with the property to adsorb a single oxygen atom upon nitrous oxide decomposition [22,23]. Although their exact structure remains unknown, the close proximity of such sites to the zeolite framework has been stressed [24–27]. Two main preparation routes for active Fe/MFI catalysts have been described, i.e., (i) controlled removal of framework Fe species of isomorphously substituted MFI-type zeolites [25, 28–37], and (ii) postsynthesis dispersion of Fe^{3+} through ion exchange of iron-containing compounds either in solution or in the gas phase [9,10,12,13,38–47]. The first method guarantees a high dispersion of iron which results in selective and stable catalysts for phenol production. The postsynthesis introduction of iron, mainly via gas-phase deposition of $FeCl_3$ followed by extensive washing to remove the chloride, has also been extensively employed. This sublimation method offers the possibility of obtaining overexchanged ZSM-5 catalysts, the term "overexchanged" stressing the iron content in excess of the expected $Fe^{n+}/Al = 1/n$ with $n = 2$ or 3. Materials prepared using this method are interesting due to their high activity in the selective reduction of NO_x. Benzene oxidation has been described less frequently for these materials and appears to be less preferred due to lower phenol selectivities [48]. There are conflicting views on the nature of the Fe species in iron-containing MFI zeolites prepared by this method. On the one hand, the heterogeneous nature of such samples has been stressed [9,10,36,46] with particles of different nuclearity including large iron oxide particles on the external surface, neutral iron oxide (FeO_x) nanoparticles in the micropores, and iron complexes (mono-, bi-, oligo-nuclear) at cation-exchange positions. On the other hand, several authors have pointed out that rather well-defined structures are obtained via the sublimation method in the precursor [42–45,47,49] which are retained upon careful calcination, resulting in the dominant presence of binuclear iron oxo complexes. This finding is based on the observation of Fe–Fe coordination numbers derived from *K*-edge EXAFS measurements close to unity [42–45,47]. As extensively outlined by Panov and co-workers [22,23], the specific catalytic property of the presumed binuclear cluster is the abstraction of one oxygen atom from a nitrous oxide molecule. In view of this specificity for nitrous oxide, the relevance of such binuclear clusters for nitric oxide reduction remains to be determined.

We have recently shown that a rather unconventional high-temperature treatment of Fe/ZSM-5 prepared by gas-phase sublimation of $FeCl_3$ results in a strong increase of the nitrous oxide decomposition rate [9]. In short, calcination and especially steaming at 973 K result in increased decomposition rates. IR spectroscopic investigations indicate that iron oxide species react with Brønsted protons to cationic Fe species upon high-temperature calcination, the protolysis reaction being reversible by hydrothermal treatment at relatively low temperature, i.e., 773 K [10]. In the present contribution, we aim to obtain further insight into the changes in the active phase and zeolite matrix upon such severe treatments. The catalysts are extensively characterized (FTIR, ^{27}Al NMR, UV–vis and ^{57}Fe Mössbauer spectroscopy, nitrogen adsorption, transmission electron microscopy, isopropylamine decomposition, and low-temperature nitrous oxide decomposition). The catalytic performance for the decomposition of nitrous oxide, the nitrous-oxide-mediated hydroxylation of benzene to phenol, and selective reduction of NO with *i*-butane is discussed in a companion paper [50].

2. Experimental

2.1. Materials

NH_4ZSM-5 (Akzo Nobel, Si/Al = 19.4) was calcined at 823 K for 2 h to obtain HZSM-5. Anhydrous $FeCl_3$ (Aldrich, reagent grade 99.9%) was sublimed onto the acid zeolite as described by Chen and Sachtler [39,51]. The temperatures of the iron precursor and zeolite were 573 and 593 K, respectively. Subsequently, the sample was washed in 2500 ml deionized water twice by stirring for 1 h each time. After drying in an oven at 383 K overnight, 1 g of the resulting material was calcined in 20 vol% O_2 in He at a flow rate of 200 ml min^{-1} while heating to 823 K at a rate of 2 K/min followed by an isothermal period of 3 h. The calcined material is denoted as Fe/ZSM-5.

Two additional samples were prepared from Fe/ZSM-5 in the following ways: (i) an amount of Fe/ZSM-5 was calcined in an artificial air flow (200 ml min^{-1}, 20 vol% O_2 in He) at 973 K for 3 h (denoted as Fe/ZSM-5(HTC); HTC, *high-temperature calcined*) and (ii) an amount of Fe/ZSM-5 was steamed (200 ml min^{-1}, 20 vol% O_2 and 10 vol% water vapor in He) at 973 K for 3 h (Fe/ZSM-5(HTS); HTS, *high-temperature steamed*). Starting from the calcined parent zeolite (HZSM-5), HZSM-5(HTC) and HZSM-5(HTS) were also prepared via similar pretreatment methods. Fe/SiO_2 was prepared by pore-volume impregnation of high-surface-area silica (Grace) with $Fe(NO_3)_3 \cdot 9H_2O$ (Merck).

2.2. Catalyst characterization

The elemental composition (Si, Al, and Fe) was determined by ICP-OES after the sample was dissolved in a mixture of HF and HNO_3. Powder X-ray diffractograms were measured using a Rigaku diffractometer. Typically, an XRD spectrum was recorded in the range $5° < 2\theta < 50°$ using Cu-K_{α_1} radiation with a scanning speed of 0.01° min^{-1}.

Infrared spectra of self-supporting 10-mg catalyst wafers were recorded at room temperature on a Bruker IFS113 Fourier transform IR spectrometer with a DTGS detector at a resolution of 4 cm^{-1}. Prior to IR measurements, the catalyst was pretreated at 773 K for 1 h in vacuo (pressure lower than 1×10^{-6} mbar) and cooled to room temperature. Normalization of the overtones of the zeolite lattice vibrations (1870–1950 cm^{-1}) was applied to quantitatively compare the number of Brønsted acid sites in the various samples. UV–vis reflection spectra were recorded at ambient temperature on a Shimadzu UV-2401 with a 60-mm integration sphere. $BaSO_4$ was used as reference material. Solid-state ^{27}Al magic-angle spinning NMR spectra were obtained on a Bruker Ultrashield 500 spectrometer at a magnetic field of 11.7 T equipped with a 4-mm MAS probe head. The Al resonance frequency at this field is 130 MHz. The sample rotation speed was 12.5 kHz. The ^{27}Al chemical shifts were referenced to a saturated $Al(NO_3)_3$ solution. Nitrogen adsorption at 77 K was carried out in a Micromeritics ASAP 2000 apparatus. Prior to nitrogen adsorption, samples were evacuated at 623 K for 16 h.

For transmission electron microscopy, a catalyst sample was mounted on a microgrid carbon polymer supported on a copper grid by placing a few droplets of a suspension of ground sample in ethanol on the grid, followed by drying at ambient conditions. High-resolution transmission electron microscopy (HRTEM) was performed using a Philips CM30ST electron microscopes with a field emission gun as the source of electrons at 300 kV. EDX elemental analysis was performed using a LINK EDX system.

Fe K-edge XAFS measurements were performed at beamline 17C of the National Synchrotron Radiation Research Center in Hsinchu (Taiwan). The electron energy and ring current were 1.5 GeV and 160 mA, respectively. The spectra were recorded with sampling steps of 0.5 eV in the XANES region and of 1 to 2 eV in the EXAFS region. An amount of catalyst was pressed into a self-supporting wafer, calculated to have an absorbance μx of 2.5, and placed in a controlled atmosphere transmission cell. Prior to measurement, the sample was heated at a rate of 2 K min^{-1} to 673 K in a flow of 20 vol% O_2 in He to remove physisorbed water. Fe K-edge spectra were recorded in transmission mode at ambient temperature in He atmosphere. EXAFS data were extracted from the measured absorption spectra with the XDAP code [52]. The preedge was subtracted using a modified Victoreen curve, while the background was subtracted by using cubic spline routines. Finally, normalization took place by dividing the subtracted absorption spectra by the intensity of the absorption spectrum at 50 eV above the Fe K-edge. Structural information was determined by multiple-shell fitting in R space [53]. The fits were checked by k^1 and k^3 weighting. Errors in the obtained numerical values are estimated ±10% for the coordination numbers (N), ±1% for the coordination distances (R), ±5% in the Debye–Waller factor ($\Delta\sigma^2$), and ±10% in the inner-potential correction (ΔE_0). Two references were used, ferric acetylacetonate for Fe–O and α-Fe_2O_3 for Fe–Fe generated by FEFF7 according to parameters provided by Battiston et al. [47].

^{57}Fe Mössbauer spectra were measured on a constant acceleration spectrometer in a triangular mode using a ^{57}Co:Rh source. All Mössbauer spectra have been recorded at 300 K, both in air and under high vacuum conditions (pressure lower than 1×10^{-6} mbar), at 77 K (pressure lower than 1×10^{-6} mbar) and at 4.2 K under high vacuum. The overall spectra were deconvoluted with calculated Mössbauer spectra that consisted of Lorentzian-shaped lines. In the case of quadrupole doublets the linewidths and the absorption areas of the constituent lines were constrained equally. Positional parameters were not constrained in the fitting procedure. The isomer shift values are reported relative to sodium nitroprusside.

Temperature-programmed decomposition of adsorbed isopropylamine (IPA) was used to determine the amount of acidic sites. In a typical experiment, 100 mg of catalyst was dried in a He flow of 100 N ml min^{-1} while heating at a rate of 2 K min^{-1} to 723 K. The sample was kept at this temperature for 1 h and subsequently cooled to 323 K. A He flow saturated with IPA at 273 K was led over the catalyst bed until no further adsorption was observed by online mass spectrometry. Subsequently, the larger part of physisorbed IPA was removed by purging in a helium flow for 16 h at 323 K. Temperature-programmed decomposition of IPA was started by heating the sample at a rate of 5 K min^{-1} to 773 K. The number of acidic sites was calculated from the number of propene molecules deriving from IPA decomposition. Special attention was paid to correct for the desorption of residual IPA which also yields a propene fragment during mass spectrometric analysis. Kofke et al. [54] have demonstrated that exactly one IPA molecule is chemisorbed per acidic site.

The low-temperature (523 K) decomposition of nitrous oxide was carried out in a static vacuum setup equipped with an online mass spectrometer for determining the gas-phase composition. A catalyst sample (typically 0.6 g) was placed into a quartz reactor tube and subjected to the following treatment: heating to 823 K in 30 min in vacuo followed by an isothermal period of 30 min, a treatment for 1 h in 1.3 mbar of oxygen, and cooling to 523 K in oxygen. After evacuation of the setup, the catalyst was exposed to a known amount of nitrous oxide (typically 2×10^{19} molecules N_2O). In a typical experiment, dinitrogen formation was observed without the production of dioxygen. This allows calculation of the number of stoichiometrically deposited oxygen atoms [22,55,56]. For higher accuracy, also isotopic exchange of the adsorbed ^{16}O with $^{18}O_2$ was carried out. To this end, the sample saturated with oxygen atoms was cooled to 323 K. After evacuation, $^{18}O_2$ (purity 95%) was admitted to the catalyst. The exchange of the two types of oxygen was followed and the number of initially deposited oxygen atoms was calculated from the equilibrium composition. We note that predominantly monoatomic exchange took place for all samples. Subsequently, a third method was applied which

Table 1
Catalyst loading as determined by ICP analyses

Sample	Al (wt%)	Fe (wt%)	Si/Al ratio	Fe/Al ratio
NH_4ZSM-5	1.79	0.024	19.4	0.0063
Fe/ZSM-5	1.79	3.68	19.4	0.97
Fe/ZSM-5(HTC)	1.79	3.68	19.4	0.97
Fe/ZSM-5(HTS)	1.79	3.68	19.4	0.97
Fe/SiO_2	0.00	3.0	–	–

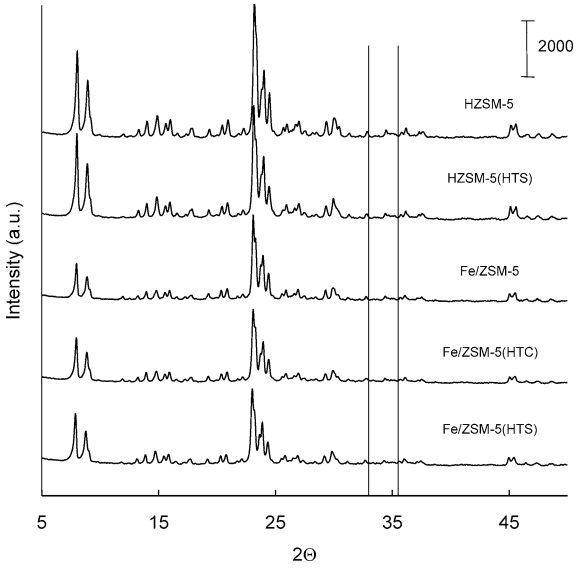

Fig. 1. Powder X-ray diffractograms of the parent zeolite HZSM-5, the steam-treated parent zeolite, and Fe-loaded materials. The dominant reflections of α- and γ-Fe_2O_3 are indicated by the solid lines.

consisted of heating the sample up to 723 K while recording the amount of released oxygen. A comparison was made of the results of these three methods.

3. Results and discussion

3.1. ICP analysis and X-ray diffraction

Table 1 reports the elemental composition of the various catalysts. The Si/Al ratio of the parent zeolite is 19.4, while it contains a small amount of iron (0.024 wt%). Fe/ZSM-5 contains 3.7 wt% Fe corresponding to a Fe/Al ratio of 0.97. Further treatment (high-temperature calcination or steaming) does not lead to loss of iron.

The X-ray diffractograms of the various samples are collected in Fig. 1. All samples exhibit the typical diffraction pattern of the MFI framework. No indications for the formation of α-Fe_2O_3 (major reflections at $2\theta = 33.2$ and 35.7°) or any other iron oxide were observed.

3.2. Infrared spectroscopy

Fig. 2 displays infrared spectra of the hydroxyl region of the various Fe-containing and parent zeolites. For HZSM-5, the bands of bridging hydroxyl groups (3613 cm^{-1}), silanol groups (3745 cm^{-1}), and a weak band (3665 cm^{-1}) assigned to the hydroxyl groups connected to extraframework aluminum species can be clearly distinguished. While the deposition of $FeCl_3$ results in the disappearance of all bridging hydroxyl groups in the parent zeolite [39], further treatment (hydrolysis, drying, and calcination at 723 K) results in restoration of about 50% of the original Brønsted site density. After calcination at 973 K, the band at 3613 cm^{-1} has further decreased in intensity and we calculate that approximately 15% of the original Brønsted acid sites persist in Fe/ZSM-5(HTC). We note here that the disappearance of these protons is reversible to some extent by exposure to water vapor at 773 K as described in an earlier communication [10]. A similar, but more pronounced decrease is observed after steaming of Fe/ZSM-5, with approximately 10% of the acid protons remaining. In this case, a small but noticeable increase in the band at 3665 cm^{-1} points to partial dealumination of the zeolite structure. A comparison of the hydroxyl band region of HZSM-5, HZSM-5(HTC), and HZSM-5(HTS) shows that dehydroxylation is relatively small upon high-temperature calcination, but extensive in the case of high-temperature steaming (around 90%).

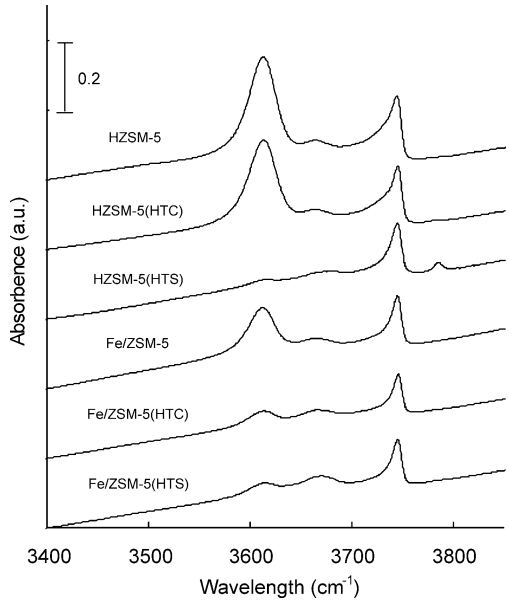

Fig. 2. Infrared spectra of the hydroxyl region of dehydrated parent materials and sublimed zeolites. Quantitative comparison of the changes of the band at about 3610 cm^{-1} was possible by normalization of the overtones of the zeolite lattice vibrations (1870–1950 cm^{-1}).

3.3. UV–vis spectroscopy

The UV–vis spectra of the two reference materials, Fe–silicalite and Fe/SiO_2, and of the HZSM-5 materials are presented in Figs. 3a and 3b, respectively. Fe–silicalite exhibits two major bands around 46,000 and 41,000 cm^{-1}, corresponding to the $t_1 \rightarrow t_2$ and $t_1 \rightarrow e$ transitions of FeO_4 tetrahedra [32,57]. This strongly indicates that all iron species

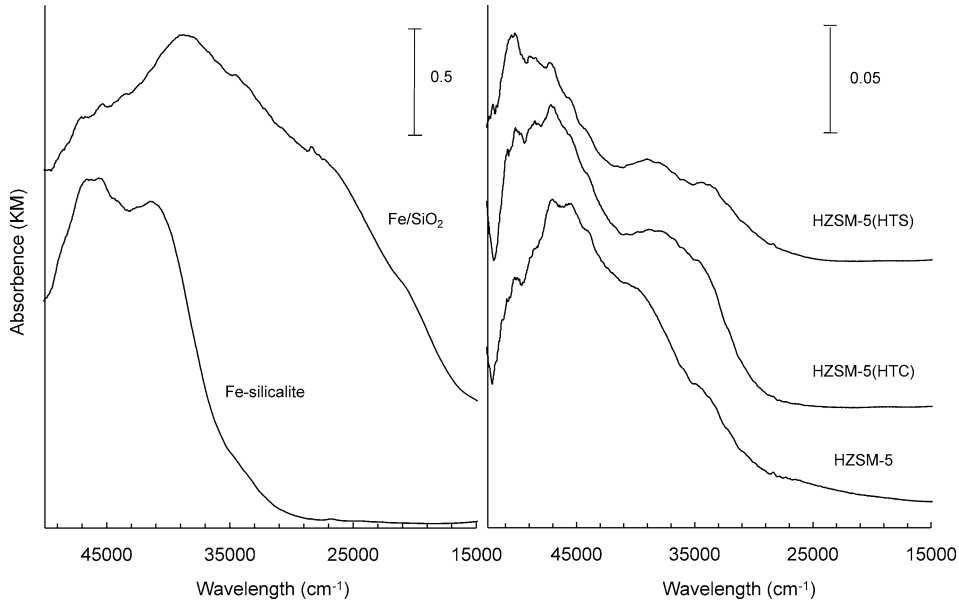

Fig. 3. UV–vis spectra of (left) Fe–silicalite and Fe/SiO_2 and (right) HZSM-5, HZSM-5(HTC), and HZSM-5(HTS).

occupy lattice positions in this sample. We note that the template was not removed in Fe–silicalite, because this would lead to partial removal of Fe from framework positions. The silica-supported iron oxide sample (Fe/SiO_2) exhibits various bands. The most dominant band at 38,574 cm^{-1} is due to small clusters of iron oxide [57]. The poorly resolved peak at 27,626 cm^{-1} may be related to iron in γ-FeOOH species [32]. The shoulder around 20,000 cm^{-1} is due to an asymmetric peak of large iron oxide aggregates. The UV–vis spectrum of HZSM-5 (Fig. 3b) indicates that this material contains a small amount of iron in accordance with the elemental analysis. Clearly, the majority of the few Fe species are tetrahedrally coordinated iron species as evidenced by the charge transfer band around 46,800 cm^{-1}. However, the band around 39,000 cm^{-1} points to the formation of small clustered Fe^{3+} species, most probably deriving from dislodgement of iron from the framework during template removal. This is underpinned by a visual comparison with the spectrum for Fe–silicalite. After high-temperature calcination and steaming, the intensity of the charge-transfer band corresponding to tetrahedrally coordinated iron, close to 46,800 cm^{-1}, decreases strongly after steaming, indicating the migration of additional framework Fe atoms to extraframework positions. Concomitantly, an increase of the band at 39,000 cm^{-1} is observed deriving from an increased contribution of small extraframework iron oxide clusters. The absence of bands around 20,000 cm^{-1} indicates that no bulky iron oxide particles are formed. The UV–vis spectra of the sublimed samples are presented in Fig. 4. Fe/ZSM-5 contains a poorly resolved band (around 45,000 cm^{-1}) assigned to tetrahedrally coordinated Fe species. An unambiguous interpretation of the band at 39,000 cm^{-1} is difficult. It is close to the band found for Fe/SiO_2 at 38,574 cm^{-1} which corresponds to small clustered Fe species [57]. The spectrum resembles the one reported by Centi et al. [57] for a

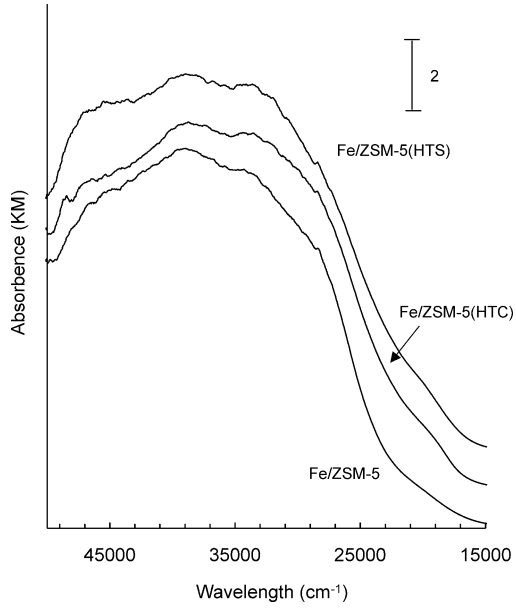

Fig. 4. UV–vis spectra of the various sublimed zeolites.

similarly prepared sample, although in their case the band around 45,000 cm^{-1} is more pronounced. Our spectrum is much more diffuse than the well-defined UV–vis spectrum obtained by Marturano et al. [44]. A poorly resolved peak at 28,207 cm^{-1} is related to iron in mixed tetra- and octahedral coordination. The absence of a band around 20,000 cm^{-1} indicates that no bulk iron oxide agglomerates are formed after mild calcination. For Fe/ZSM-5(HTC), the poorly resolved band around 20,000 cm^{-1} points to the formation of larger iron oxide species. Steaming of Fe/ZSM-5 causes further redistribution of the band intensities and widths. The contribution of the band corresponding to clustered Fe species

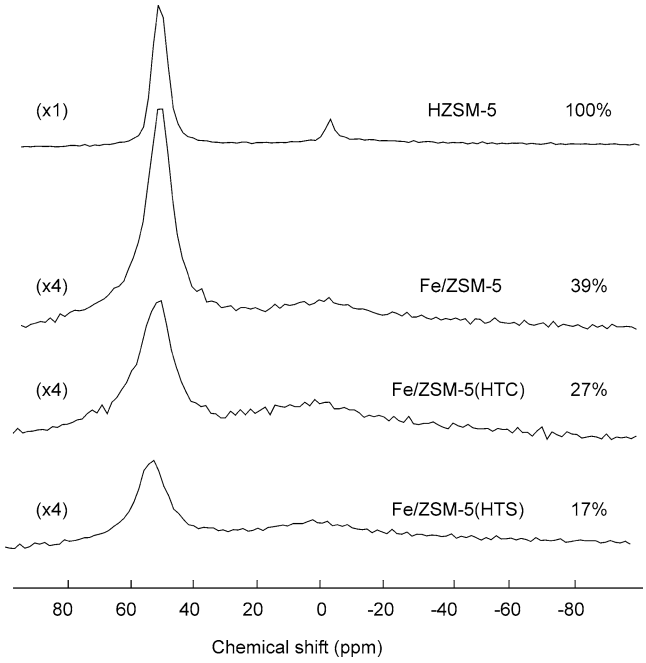

Fig. 5. ^{27}Al MAS NMR spectra of the HZSM-5 material (1024 scans) and those obtained after sublimation and further treatment (4096 scans). The fraction of visible aluminum (signal at 54 ppm) compared to the total signal in the original material is also indicated.

becomes larger. Steaming also causes an increased contribution of large iron oxide aggregates.

3.4. ^{27}Al nuclear magnetic resonance

^{27}Al MAS NMR spectra were recorded for the three sublimed samples. The spectra are reported in Fig. 5 together with the spectrum of HZSM-5. This latter spectrum contains a dominant resonance at 54 ppm assigned to tetrahedrally coordinated Al in lattice positions. Additionally, a small amount of extraframework Al with octahedral coordination resulting in a resonance at 0 ppm is present. The resonance at 54 ppm is strongly reduced in Fe/ZSM-5. This is due to the paramagnetism of iron. The local magnetic field generated by its unpaired electrons strongly perturbs the resonance of the ^{27}Al nuclei. Also, the sharp resonance at 0 ppm is transformed into a broad signal around this value. Although difficult to ascertain, some dealumination might have taken place in line with the report by Marturano et al. [43]. Quantification of the areas of the resonance at 54 ppm for HZSM-5 and Fe/ZSM-5 shows that only about 39% of the original tetrahedral Al signal is observed in the sublimed sample. This observation points to a close proximity of Fe species to Al sites and provides a tentative explanation for the decrease of the intensity of the IR band corresponding to bridging hydroxyl groups. The decrease of the resonance signal at 54 ppm is even more pronounced in Fe/ZSM-5(HTC) and Fe/ZSM-5(HTS), leaving about 27 and 17% of the aluminum detected, respectively. This again parallels the IR observations and is in line with our earlier report of a protolysis reaction between iron oxide particles and Brønsted protons upon high-temperature calcination which is reversible [10]. Steaming results in a stronger decrease of the resonant signal at 54 ppm and extensive removal of Al from lattice positions is assumed to take place. Most importantly, we conclude that high-temperature treatments lead to a closer proximity of Fe and Al in sublimed catalysts. During high-temperature calcination, this is primarily due to the protolysis reaction between small iron oxide particles and the Brønsted acid sites. This results in charge compensation of the negative framework charge by iron-containing oxo cations, in the simplest form a $[Fe{=}O]^+$ cation. On the other hand, high-temperature steaming will definitely result in the extraction of Al from lattice positions and the possibility of the formation of extraframework mixed iron–aluminum–oxo species should be considered.

3.5. Nitrogen adsorption

The textural properties of the catalyst samples (HZSM-5 and the sublimed samples) were investigated by nitrogen adsorption. The isotherms all exhibit Type I adsorption isotherms as expected for microporous solids. The BET method, based on multilayer N_2 adsorption, is inadequate to describe the adsorption process in medium-pore zeolites due to the restricted pore sizes. This is exemplified by the fact that we derived negative C values for all isotherms. For a qualitative analysis of the isotherms, the Langmuir equation and the Dubinin–Radushkevich (D–R) and Dubinin–Astakhov (D–Ast) methods were employed [58]. The results collected in Table 2 for HZSM-5 and Fe/ZSM-5 clearly point to the incorporation of species into the micropore space of HZSM-5. This is reflected by the lower surface area and micropore volume. The large decrease is most probably related to some degree of pore blocking. The increase in micropore volume ($V_{\mathrm{D-Ast}}$) for Fe/ZSM-5(HTC)

Table 2
The surface area (S_{Lang}) and micropore volume (V_{Lang}) derived from the Langmuir equation, the micropore surface area ($S_{\mathrm{D-R}}$), and micropore volume ($V_{\mathrm{D-R}}$) calculated using the Dubinin–Radushkevich method and the Dubinin–Astakhov limiting micropore volume ($V_{\mathrm{D-Ast}}$)

Sample	S_{Lang} ($m^2\,g^{-1}$)	V_{Lang} ($cm^3\,g^{-1}$)	$S_{\mathrm{D-R}}$ ($m^2\,g^{-1}$)	$V_{\mathrm{D-R}}$ ($cm^3\,g^{-1}$)	$V_{\mathrm{D-Ast}}$ ($cm^3\,g^{-1}$)
HZSM-5	440	0.16	417	0.15	0.17
Fe/ZSM-5	334	0.12	340	0.12	0.13
Fe/ZSM-5(HTC)	341	0.12	337	0.12	0.13
Fe/ZSM-5(HTS)	371	0.13	359	0.13	0.14

points to a redistribution of iron species, most probably related to their size. This is also suggested by the almost similar values for V_{D-R} of Fe/ZSM-5 and Fe/ZSM-5(HTC) and may point to changes in the nature of extraframework species rather than to changes in the pore structure. The latter type of changes is not expected since dealumination of HZSM-5 upon high-temperature calcination appears to be small. Steaming, however, results in a significant increase in the surface area and pore volume as derived by the different analysis methods. This points to the creation of larger pores occurring concomitant with removal of aluminum from lattice positions. Alternatively, this can be taken as an indication of the migration of small iron species from the micropores to the external surface.

3.6. Transmission electron microscopy

Fig. 6 shows representative TEM micrographs of Fe/ZSM-5 and its high-temperature calcined and steamed counterparts. All three samples clearly show the presence of iron oxide particles on the external zeolite surface as confirmed by EDX analysis. The presence of iron oxide particles on the external zeolite surface was noted before by Chen and Sachtler [39], although the particles appear to be smaller in the present study. The exact distribution of Fe species is strongly dependent on the calcination procedure [39,46,47]. The size of the particles strongly suggests that these particles are mainly located on the external surface but one has to take into account the possibility that aggregates can be located in the near-surface region of the zeolite as shown for mildly calcined materials by an elemental EELS/STEM map [47]. Heinrich et al. [46] suggested that such particles can further grow in the near-surface region and partially destroy the lattice under more severe conditions. While the iron oxide particles are quite homogeneously distributed over the surface with dimensions of 1–4 nm in the case of Fe/ZSM-5 with some larger particles up to 10 nm present, they tend to sinter further upon high-temperature treatments. This results in a predominance of particles in the range of 2–10 nm, but also particles in the range 10–50 nm are found. Especially, steaming results in the formation of larger agglomerates. Most probably, the effect of water induces a higher mobility of iron oxide species, which may provide a partial explanation for the relatively strong increase in micropore volume upon steaming.

3.7. Fe K-edge X-ray absorption spectroscopy

Fig. 7 provides a comparison of the near-edge regions of the X-ray absorption spectra of α-Fe_2O_3, γ-Fe_2O_3, and the three sublimed catalysts. The edge positions of the Fe/ZSM-5 catalysts agree well with those in the reference oxides, indicating the predominant presence of Fe^{3+}. The preedge absorption feature due to a $1s \rightarrow 3d$ transition is forbidden for octahedral coordination but arises in distorted octahedral and tetrahedral symmetries. For γ-Fe_2O_3 with 50%

(a)

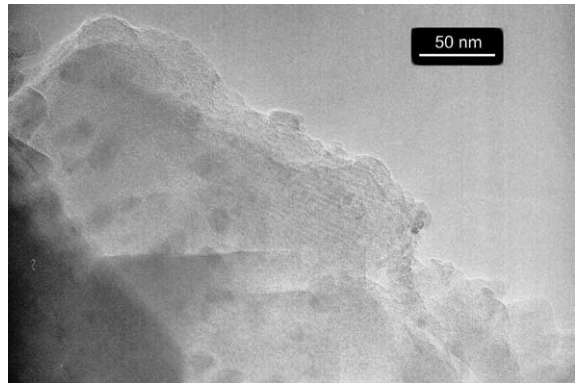

(b)

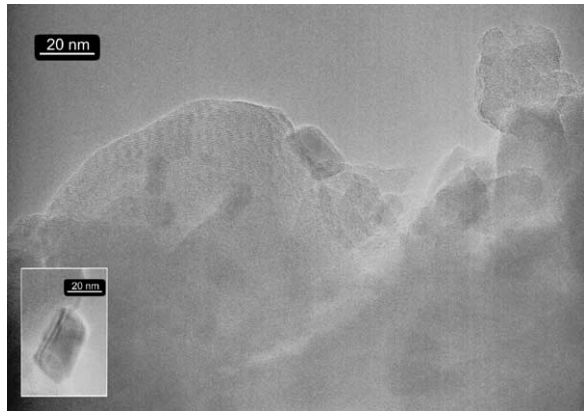

(c)

Fig. 6. Transmission electron micrographs of (a) Fe/ZSM-5, (b) Fe/ZSM-5(HTC), and (c) Fe/ZSM-5(HTS) showing the presence of iron oxide particles on the external surface. The presence of Fe in these particles was confirmed by EDX analysis. The inset on the micrograph of Fe/ZSM-5(HTS) shows a relatively large iron oxide particle, frequently observed for this sample.

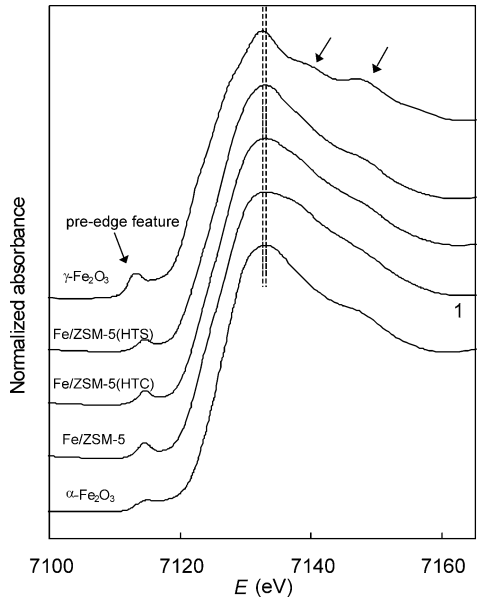

Fig. 7. XANES at the Fe K-edge for α-Fe_2O_3, γ-Fe_2O_3, and the sublimed catalysts after in situ calcination.

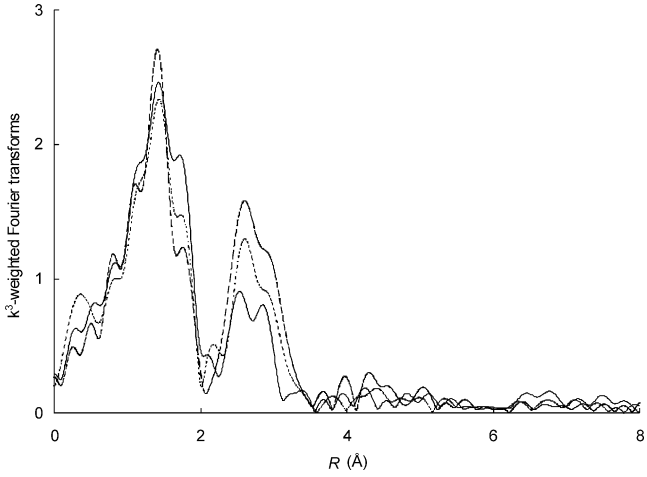

Fig. 8. Absolute part of the k^3-weighted spectra for Fe/ZSM-5 (solid line), Fe/ZSM-5(HTC) (dotted line), and Fe/ZSM-5(HTS) (dashed line).

of Fe^{3+} in tetrahedral symmetry this feature is more intense than for Fe^{3+} in distorted octahedral symmetry as in α-Fe_2O_3 [59]. In line with the recent report by Heinrich et al. [46], all three catalyst samples show a preedge feature intermediate between those of the two reference oxides. This points to the presence of tetrahedral Fe^{3+}, although its contribution should be less than 50%. Moreover, the scattering features just above the absorption maximum become more pronounced for the catalysts which have been severely treated. In particular the steamed sample shows a pronounced order in the higher coordination spheres in line with the results from EXAFS data analysis (vide infra). Fig. 8 shows the absolute part of the k^3-weighted spectra for the catalyst samples. Clearly, the samples do not differ to a great extent from each other except for the intensities. Multiple shell analysis of these EXAFS data was performed taking

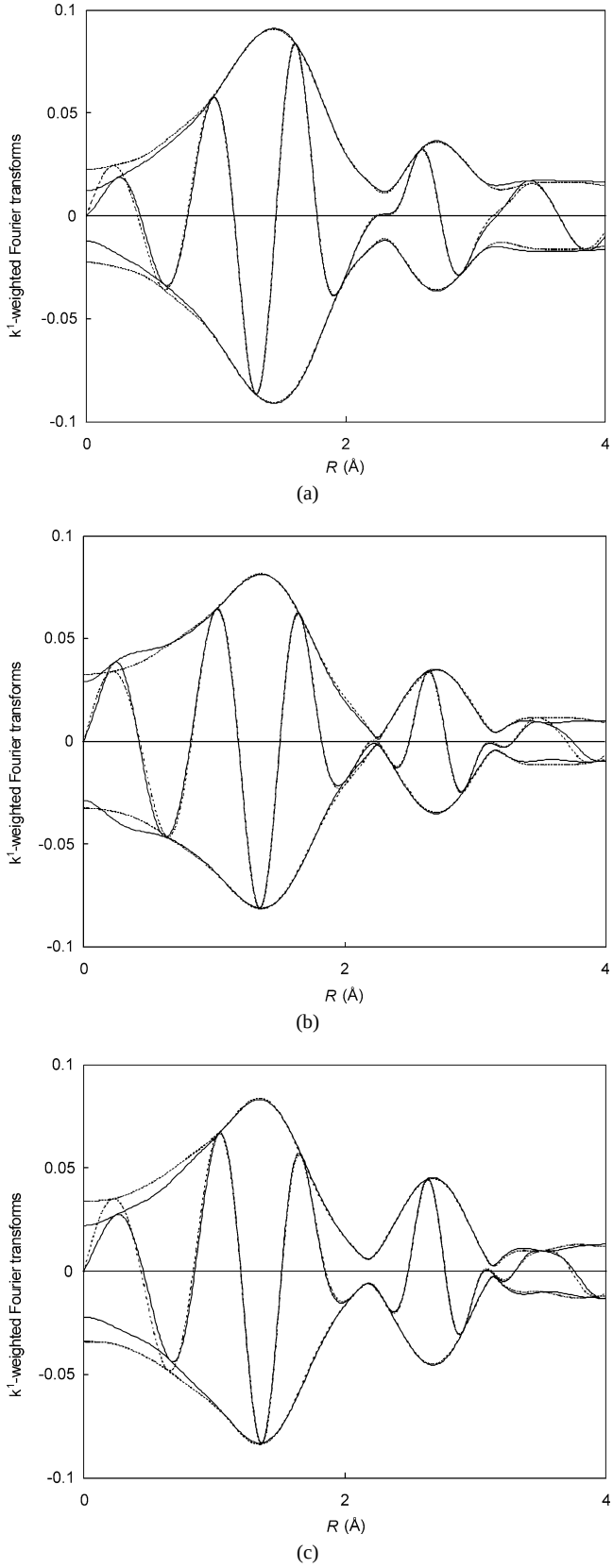

Fig. 9. k^1-Fourier-transformed experimental (solid line) and fitted (dashed line, R = 1–4 Å, Δk = 2.7–12) data for (a) Fe/ZSM-5, (b) Fe/ZSM-5(HTC), and (c) Fe/ZSM-5(HTS).

Table 3
Fit parameters of multiple shell analysis of the EXAFS data for Fe/ZSM-5, Fe/ZSM-5(HTC), and Fe/ZSM-5(HTS)

Shell	CN	R	$\Delta\sigma^2$	ΔE_0	k^1-Variance (%)	
		(Å)	(10^{-3} Å^2)	(eV)	Im. part	Abs. part
Fe/ZSM-5					0.07	0.04
Fe–O_1	3.0	1.87	3.46	−4.57		
Fe–O_2	3.0	1.99	1.68	6.33		
Fe–Fe_1	1.2	2.93	6.24	−8.46		
Fe–Fe_2	0.9	3.32	3.58	9.70		
Fe–O_3	1.2	3.91	11.2	−3.53		
Fe/ZSM-5(HTC)					0.14	0.06
Fe–O_1	3.3	1.88	2.85	0.05		
Fe–O_2	2.8	2.01	1.33	11.90		
Fe–Fe_1	1.4	2.93	6.39	−1.54		
Fe–Fe_2	1.2	3.36	3.64	5.39		
Fe–O_3	1.2	3.91	10.9	−3.51		
Fe/ZSM-5(HTS)					0.06	0.02
Fe–O_1	3.0	1.89	1.96	0.54		
Fe–O_2	3.0	2.01	6.11	12.06		
Fe–Fe_1	1.8	2.97	6.11	−8.50		
Fe–Fe_2	1.1	3.36	1.53	4.87		
Fe–O_3	1.6	4.13	11.6	−10.1		

into account the models postulated by Battiston et al. [47]. In particular, we used their result that the first oxygen shell can be fitted by six oxygen atoms at two different distances. In agreement with their results, this led to better fit results than the use of three different Fe–O shells. Moreover, a third Fe–O shell at a larger distance ($R = 3.9$–4.2 Å) considerably improved the fitting results. The k^1-weighted Fourier transform and the corresponding best fit for Fe/ZSM-5 are presented in Fig. 9a. The fit results are collected in Table 3. Two oxygen shells were fitted producing a total Fe–O coordination number (CN) of six in the first shell. The second shell consists of two Fe–Fe contributions, because fitting with one Fe–Fe shell did not produce satisfactory results. The coordination number of the Fe–Fe_1 shell is 1.2 while a value of 0.9 is found for the Fe–Fe_2 shell. The results for the first shell are close to those reported recently by Battiston et al. [47] for similar samples and to some extent to those by Marturano et al. [43,44]. Most notably, the CN of the two Fe–Fe shells in the Fe/ZSM-5 sample of the present work are between those of samples obtained after mild calcination and severe calcination in the study of Battiston et al. [47]. Given that our calcination procedure for Fe/ZSM-5 is of intermediate severity, the somewhat higher value for the coordination number of the Fe–Fe_2 shell is in rather good agreement with these earlier results. On the other hand, the coordination distances are somewhat lower and appear to agree better with the results of Heinrich et al. [46]. Figs. 9b and 9c produce the k^1-weighted Fourier transforms and best fits for Fe/ZSM-5(HTC) and Fe/ZSM-5(HTS), respectively. Large changes are observed for the two Fe–Fe shells, whereas the first iron–oxygen shell remains unaltered. The fit results indeed show that there are no large changes in this latter shell. The coordination numbers for the two Fe–Fe shells strongly increase upon high-temperature treatments. This points to further ordering and/or particle growth of the iron oxide phases. This qualitatively agrees with the observations of Battiston et al. [47] comparing mildly and severely calcined Fe/ZSM-5 precursors. While the quite severe calcination temperature has led to the segregation of a large part of iron into iron oxide particles, the low coordination numbers for the Fe–Fe shell for Fe/ZSM-5 are attributed to structural disorder of the iron oxide aggregates. Increasing severity of treatment induces a further growth and ordering of such particles, which is reflected by increasing Fe–Fe coordination numbers. This notion is in line with the presence of clustered iron oxide particles observed by UV–vis spectroscopy and of large iron oxide aggregates observed by TEM and derived from ^{57}Fe Mössbauer spectroscopy (vide infra).

3.8. ^{57}Fe Mössbauer spectroscopy

Fig. 10 displays ^{57}Fe Mössbauer absorption spectra (MAS) of three Fe/ZSM-5 catalysts recorded at 300 K, in air (only shown for the steamed sample) and under high-vacuum conditions, and at 77 and 4.2 K under high-vacuum conditions. The complex nature of the spectra points to the presence of several species. At 300 K one doublet with an isomer shift (IS) of 0.61 mm s^{-1} and a quadrupole splitting (QS) of 1.02 mm s^{-1} is detected for Fe/ZSM-5. This well-resolved doublet means that the Fe phase is relatively dense (no paramagnetic hyperfine splitting is observed), but it also indicates that the iron oxide particles are smaller than about 6 nm. This component is also present in the high-temperature calcined sample. Additionally, one observes the onset of a six-line pattern indicative for the presence of a high-spin Fe^{3+} contribution. This is the result of the superparamagnetic behavior of relatively large iron oxide particles. A small shoulder can be observed on the high-energy line of the Fe^{3+} doublet. The fit parameters (IS = 1.33 mm s^{-1} and QS = 3.19 mm s^{-1}) point to the presence of Fe^{2+}. This Fe^{2+} component is also present in the steamed sample, Fe/ZSM-5(HTS), under high-vacuum conditions. For Fe/ZSM-5(HTS), the Mössbauer spectrum was also recorded in air. In this case, the Fe^{2+} component was not observed. The broad singlet at 0.60 mm s^{-1} observed in Fe/ZSM-5(HTS) at 300 K can most probably be related to superparamagnetic iron oxide particles close to the superparamagnetic transition temperature. This is underpinned by the development of a sextuplet at 77 K for this sample (vide infra). Additional measurements of Mössbauer spectra at 77 and 4.2 K allow further insight into the particle-size distribution of small iron oxide particles and the relative abundance of the various Fe species. This latter point should be addressed with care, since the recoil-free fraction for clustered iron oxides may be significantly different from that of mono- or oligonuclear species. Nevertheless, we will employ the contributions of the various Fe states to the total resonant absorption area at 4.2 K as an estimate of their relative abundance. The resulting spectral fit parameters are

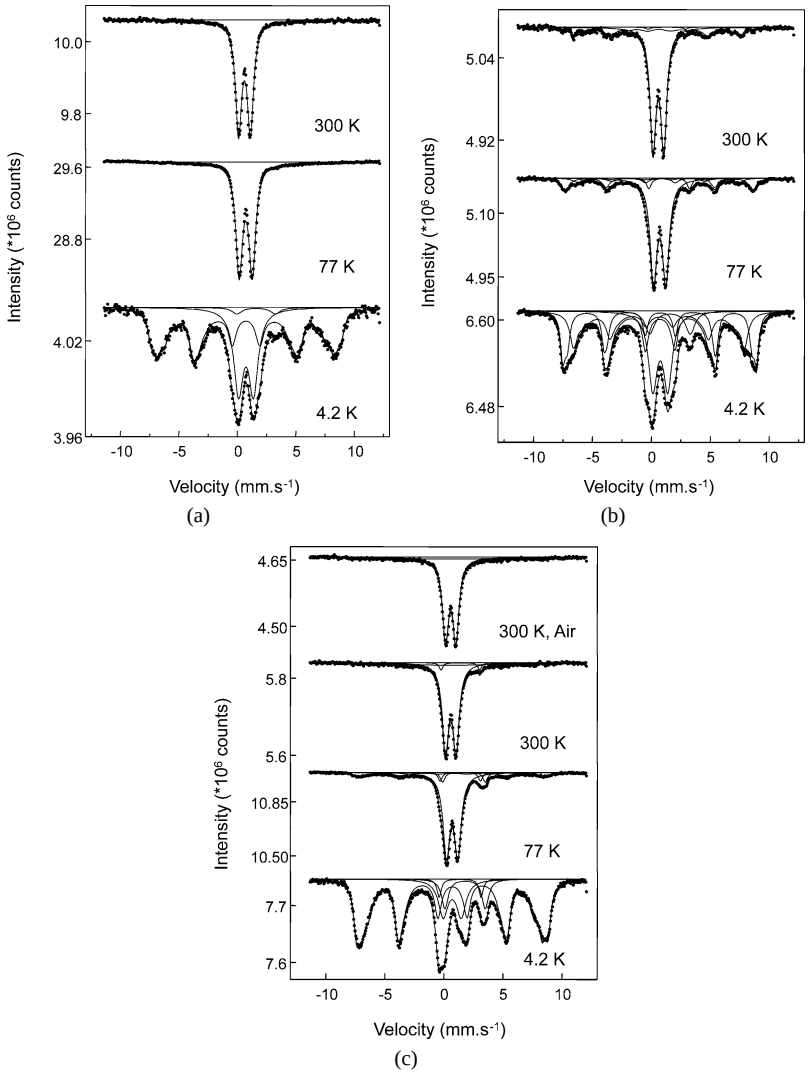

Fig. 10. ^{57}Fe Mössbauer spectra for (a) Fe/ZSM-5, (b) Fe/ZSM-5(HTC), and (c) Fe/ZSM-5(HTS). Spectra were recorded under high-vacuum conditions at 300, 77, and 4.2 K. For Fe/ZSM-5(HTS) an additional spectrum after air exposure at 300 K is displayed.

listed in Table 4. For Fe/ZSM-5, a full-grown sextuplet is only observed in the Mössbauer spectrum at 4.2 K. The absence of this pattern at a temperature of 77 K points to the presence of relatively small iron oxide particles (ca. 2 nm) in line with the TEM observations. The relatively broad lines of the sextuplet in Fe/ZSM-5 stress the amorphous character of the associated iron oxide particles, with a lower hyperfine field (45.5 T) than in bulk α-Fe_2O_3 (54.4 T at 0 K). The spectral contribution of these particles amounts to approximately 66% at 4.2 K. The Fe^{3+} doublet (IS $= 0.74$ mm s^{-1} and QS $= 1.28$ mm s^{-1}) with a spectral contribution of 31% relates to very small Fe species occluded in the zeolite micropore space. We cannot draw conclusions on the nuclearity of such species. The contribution of the Fe^{2+} doublet with fit parameters close to those obtained after fitting of the room temperature spectrum of the severely treated samples was 3%.

A broad particle-size distribution is observed for Fe/ZSM-5(HTC). Relatively large iron oxide crystallites (> 8 nm) are present as derived from the occurrence of a sextuplet in the room temperature spectrum of this sample. Additionally, the fit parameters show the presence of a relatively large fraction of 2- to 4-nm-sized particles. This qualitatively agrees with the TEM observation of some sintering of iron oxide particles on the external surface of the zeolite. The spectrum at 4.2 K clearly shows the presence of two sextuplet contributions, one with a hyperfine field of 43.1 T and one with a hyperfine field of 50.4 T. At the moment, the structure of these iron oxide phases is unclear, although the latter contribution may point to nanocrystalline α-Fe_2O_3 particles. At 4.2 K, the spectral contribution of the components related to large iron oxide particles does not significantly increase after high-temperature calcination. However, the spectral contribution of the Fe^{2+} doublet has increased significantly.

The high-temperature steamed sample, Fe/ZSM-5(HTS), presents a relatively large fraction of iron oxide particles in the range of 2–4 nm. The relative contribution of this fraction

Table 4
Mössbauer parameters and fraction of iron states in Fe/ZSM-5, Fe/ZSM-5(HTC), and Fe/ZSM-5(HTS)

Sample	Temperature (K)	Fe state	Isomer shift ($mm\,s^{-1}$)	Quadrupole splitting ($mm\,s^{-1}$)	Hyperfine field (T)	Relative intensity (%)	Amount Fe (10^{19} Fe g^{-1})
Fe/ZSM-5	300	Fe^{3+}	0.61	1.02		100	38.7
	77	Fe^{3+}	0.72	1.13		100	38.7
	4.2	Fe^{3+}	0.73	0.01	45.5	66	25.5
		Fe^{3+}	0.74	1.28		31	12.2
		Fe^{2+}	1.60	3.30		3	1.0
Fe/ZSM-5(HTC)	300	Fe^{3+}	0.60	0.06	43.6	25	9.8
		Fe^{3+}	0.60	0.91		74	28.6
		Fe^{2+}	1.33	3.19		1	0.4
	77	Fe^{3+}	0.72	0.05	47.6	28	10.7
		Fe^{3+}	0.72	1.05		67	26.0
		Fe^{2+}	1.52	3.46		5	2.0
	4.2	Fe^{3+}	0.68	0.02	43.1	33	12.7
		Fe^{3+}	0.74	0.02	50.4	31	12.0
		Fe^{3+}	0.76	1.27		27	10.6
		Fe^{2+}	1.59	3.43		9	3.4
Fe/ZSM-5(HTS)	300, air	Fe^{3+}	0.60	0.88		85	32.7
		Fe^{3+}	0.60			15	6.0
	300	Fe^{3+}	0.61	0.90		79	30.6
		Fe^{3+}	0.60			17	6.5
		Fe^{2+}	1.42	3.28		4	1.6
	77	Fe^{3+}	0.72	0.96		72	27.7
		Fe^{3+}	0.75	0.00	48.3	17	6.7
		Fe^{2+}	1.41	3.43		5	1.9
		Fe^{2+}	1.72	3.61		6	2.4
	4.2	Fe^{3+}	0.72	0.02	47.3	72	27.7
		Fe^{3+}	0.73	1.53		16	6.1
		Fe^{2+}	1.40	3.55		3	1.4
		Fe^{2+}	1.82	3.42		9	3.5

has grown slightly compared to Fe/ZSM-5. The Fe^{3+} doublet has significantly decreased in this sample. We attribute this partly to the migration of very small iron oxide particles from the zeolite pores to the external surface. The presence of water during steaming may play an important role in the higher mobility of iron oxide particles when compared to the high-temperature calcination treatment. On the other hand, also the Fe^{2+} contribution appears to increase resulting in the presence of two doublets, with the fit parameters IS = 1.40 $mm\,s^{-1}$, QS = 3.55 $mm\,s^{-1}$, and IS = 1.82 $mm\,s^{-1}$ and QS = 3.42 $mm\,s^{-1}$. The occurrence of two Fe^{2+} states was previously reported by Pérez-Ramírez et al. [60] and by Dubkov et al. [56] for activated isomorphously substituted FeZSM-5.

3.9. Isopropylamine decomposition

The number of Brønsted acid sites determined by the decomposition of isopropylamine for the various catalysts is shown in Table 5. The value for HZSM-5 (0.83 mmol $H^+\,g^{-1}$) is close to the theoretical amount corresponding to a framework Si/Al ratio of 19.4. High-temperature calcination of HZSM-5 results in a small decrease in acidity. This is in line with our earlier observation of a small decrease of the hydroxyl band at 3613 cm^{-1} (Fig. 2). On the other hand, steaming results in a substantial decrease in Brønsted acidity which is related to the removal of Al from lattice positions. The value points to the presence of quite an amount of acidic protons, although they were not observed in the hydroxyl region. Possibly, such species are perturbed by the presence of extraframework species. There is a very small contribution of protons with a lower acidity (higher decomposition temperature of IPA) which most probably relates to OH groups of extraframework species. The acid site density of Fe/ZSM-5 amounts to 0.47 mmol $H^+\,g^{-1}$. The decrease upon introduction of Fe into HZSM-5 corresponds well

Table 5
The amount of acid sites determined from isopropylamine decomposition

Sample	Number of H^+ sites ($mmol\,g^{-1}$)		
	$T = 583$ K bridging Si–O–Al	$T = 653$ K	$T = 683$ K
HZSM-5	0.83[a]	0.01	0.00
HZSM-5(HTC)	0.79	0.01	0.00
HZSM-5(HTS)	0.21	0.01	0.01
Fe/ZSM-5	0.47	0.09	0.12
Fe/ZSM-5(HTC)	0.34	0.11	0.13
Fe/ZSM-5(HTS)	0.21	0.07	0.07

[a] The calculated Brønsted acid site concentration derived from the aluminum content of the parent zeolite amounts to 0.82 $mmol\,g^{-1}$.

with the decrease derived from IR spectroscopy. Subsequent high-temperature treatments further decrease the number of protons. The decrease after high-temperature calcination is due to the protolysis reaction of small occluded neutral iron oxide particles as outlined earlier [9,10]. This also parallels the observed decrease in the resonance area of tetrahedral Al species determined from ^{27}Al NMR, explained by a closer proximity of the Al nuclei to the paramagnetic Fe centers. Steaming results in a further decrease of the acid site density (0.21 mmol $H^+ g^{-1}$). The amount of hydroxyl groups derived from infrared spectroscopy is somewhat lower. This may suggest that some protons are strongly perturbed by the presence of extraframework species, possibly iron oxide particles. Notably, the iron-containing samples clearly show the presence of two extra protonic species with a lower acidity. The absence of such contributions in the HZSM-5 samples stresses that these species are related to iron oxide particles, although their nature remains unclear at the moment.

3.10. Low-temperature nitrous oxide decomposition

Nitrous oxide decomposition at relatively low temperatures allows the stoichiometric deposition of one oxygen atom on active centers under the release of dinitrogen [22,23]. Such sites are thought to consist of binuclear Fe centers, have been coined α-sites by the group of Panov, and have been reported to be created upon high-temperature activation leading to reduction of some Fe^{3+} species to Fe^{2+} [56]. These species are stable in the presence of molecular oxygen and can be reoxidized by nitrous oxide. Table 6 lists the number of deposited oxygen atoms (N_{N_2O}) as determined by low-temperature (523 K) nitrous oxide decomposition, subsequent room temperature isotopic exchange with $^{18}O_2$ and oxygen desorption. Qualitatively, the amount of deposited oxygen atoms increases in the order: HZSM-5(HTS) < Fe/ZSM-5 < Fe/ZSM-5(HTC) < Fe/ZSM-5(HTS). The agreement between the various methods is not perfect and especially the values obtained after oxygen desorption are somewhat higher. This is most probably due to some autoreduction of aggregated iron oxide species. From a chemical point of view, the $^{18}O_2$-exchange experiments are most reliable since they relate to measurements carried out close to room temperature. It is expected that only the most reactive oxygen species are isotopically exchanged under these reaction conditions. Comparing the present results to those obtained by Dubkov et al. [56] for a sample prepared by hydrothermal synthesis, we can conclude that the amount of deposited oxygen atoms is an order of magnitude higher for our sublimed samples. This is attributed to the higher Fe content. In line with the study of Dubkov et al. [56], an increase is found with increasing treatment temperature and the presence of water vapor during pretreatment. There are several indications that the activity in nitrous oxide and benzene-to-phenol conversion correlates to sites capable of decomposing nitrous oxide at low temperatures [56]. We have reached similar conclusions [50]. Interestingly, the titration data imply that the number of Fe atoms involved in such specific sites in catalysts prepared by sublimation of $FeCl_3$ is very small. Moreover, we observe that the increase of the number of active sites for low-temperature nitrous oxide decomposition correlates with the increase of the Fe^{2+} component observed from Mössbauer spectroscopy. This appears to be in agreement with the recent strong evidence provided by Dubkov et al. [56]. We can thus forward that the increased number of active sites is linked to the increase of the number of Fe^{2+} species. It is difficult to draw pertinent conclusions on the exact number of Fe^{2+} states involved in the nitrous oxide decomposition. For instance, Dubkov et al. [56] have found that about one-third of the Fe^{2+} sites in samples with relatively low Fe content are not involved in the deposition of oxygen from nitrous oxide. We cannot draw conclusions on this fraction for our samples. A recent study by the group of Sachtler [61] has shown that also oxygen atoms of aggregated iron oxide particles can be isotopically exchanged at relatively high temperatures. We stress here that the current isotopic exchange experiments were carried out at much lower temperature and that the deposited oxygen atoms should be probed [22,55,56]. Furthermore, we note that the quantification of the Fe^{2+} component from the Mössbauer spectra which are dominated by a sextuplet of relatively large iron oxide particles is by no means very accurate, although quantification of the contribution of the various Fe species from spectra recorded at 4.2 K is more meaningful than from spectra recorded at 77 K. Nonetheless, we observe that the number of oxygen atoms deposited from nitrous oxide is in the same order as the number of Fe atoms in the 2+ oxidation state. We can thus draw the conclusion that only a relatively small part of the iron present in the sublimed samples is present as Fe^{2+} and is able to activate nitrous oxide. Another important point to note is that this fraction increases with increasing severity of treatment. A very crude analysis shows that the Fe^{2+} content amounts to 0.1 wt% for Fe/ZSM-5 and increases to 0.32 wt% for Fe/ZSM-5(HTC) and 0.45 wt% for Fe/ZSM-5(HTS). In view of the inaccuracies of the various parameters, we cannot calculate the exact nuclearity of the Fe active sites ($n = C_{Fe^{2+}}/N_{N_2O}$). The values for n (1.8 for Fe/ZSM-5, 2.2 for Fe/ZSM-5(HTC), and 2.3 for Fe/ZSM-5(HTS)) thus provide only an upper limit of n for the present set of samples. Tentatively, this agrees

Table 6
The number of sites able to decompose nitrous oxide at low temperature (523 K), the number of exchangeable deposited oxygen atoms (323 K), and the number of oxygen atoms desorbing in a TPD experiment (up to 773 K)

Sample	Number of sites (g^{-1})		
	N_2O decomposition	$^{18}O_2$ exchange	O_2 desorption
Fe/ZSM-5	8.8×10^{18}	0.58×10^{19}	1.5×10^{19}
Fe/ZSM-5(HTC)	1.6×10^{19}	1.5×10^{19}	2.0×10^{19}
Fe/ZSM-5(HTS)	2.0×10^{19}	1.9×10^{19}	1.8×10^{19}
HZSM-5(HTS)	–	5.0×10^{17}	7.2×10^{17}

with the notion of a binuclear iron complex [22,23,62–64]. Whereas earlier Panov and co-workers reached similar conclusions [65,66], Dubkov et al. [56] recently pointed out that two oxygen atoms could be accommodated on such a binuclear cluster. Assuming that n equals 2, the value obtained for the low-temperature nitrous oxide decomposition on HZSM-5(HTS) would suggest that about one-third of the total iron content in HZSM-5 (approximately 0.0083 wt% of the total content of 0.024 wt%) is associated with the active sites in this zeolite. The higher fraction of active iron for those catalysts with a lower iron content agrees with the report of Dubkov et al. [56].

Summarizing, Fe/ZSM-5 prepared by chemical vapor deposition of $FeCl_3$ followed by washing and calcination can be characterized by the predominant presence of iron oxide aggregates on the external surface. This primarily follows from a combination of TEM imaging and ^{57}Fe Mössbauer spectroscopy measurements, the latter technique showing a large contribution of iron oxide particles too large to be accommodated in the zeolite micropores. Conversely, structure analysis of Fe K-edge XAS data points to relatively low Fe–Fe coordination numbers (CN = 1.2). Both the TEM and ^{57}Fe MAS results clearly show that this cannot be explained by the predominant presence of binuclear Fe clusters. The relatively low values for the hyperfine field of the iron oxide phase identified by ^{57}Fe MAS in this sample indicate that we are dealing with a highly disordered iron oxide/hydroxide phase. The low Fe–Fe coordination number may thus be due to the disordered nature of these iron oxide particles. A recent study on supported MoS_2 particles [67] has indeed shown that disorder in small particles can result in lower metal–metal coordination numbers than is to be expected from the particle size evaluated from TEM micrographs. Our explanation contrasts earlier conclusions reached by the groups of Prins [43,44] and Koningsberger [45,47]. These authors speculated that the Fe–Fe coordination numbers close to unity point to a large fraction of binuclear Fe clusters occluded in the micropores. Battiston et al. [47] have carefully determined that a slow heating rate during calcination after washing results in a well-dispersed iron oxide phase. TEM imaging indeed showed that most of the iron species are located in the zeolite micropores, whereas more severe calcination treatments induced the preferential presence of iron in the near-surface region of the zeolite crystallites. Moreover, comparison of UV–vis spectra in Ref. [44] and in this study provides further clues that the present Fe/ZSM-5 material contains a larger fraction of larger iron oxide aggregates. Also, the fraction of nanocrystalline iron oxide particles as determined by Mössbauer spectroscopy in Ref. [47] is lower. On the other hand, the amount of Fe^{2+} in that sample is close to the amount identified for the present Fe/ZSM-5 determined under exactly the same experimental conditions, giving some indication that the amount of active sites for nitrous oxide decomposition should be equally small for both samples. These findings stress that the iron distribution in sublimed catalysts is critically dependent on the exact pretreatment and most probably also on the nature of the parent HZSM-5 zeolite material. This renders it troublesome to directly compare results from various studies. An important finding, however, is that only a small fraction of Fe sites is involved in the decomposition of nitrous oxide at low temperatures for Fe/ZSM-5 prepared by chemical vapor deposition of $FeCl_3$.

Further high-temperature treatment of Fe/ZSM-5 results in considerable changes of the intrazeolite Fe species. High-temperature calcination results in the replacement of charge-compensating protons by cationic Fe complexes. ^{27}Al NMR measurements confirm the closer proximity of the Al nuclei and paramagnetic Fe ions after high-temperature treatment. We have observed that the resonances due to both octahedral and tetrahedral Al are perturbed, which appears to be in line with the protolysis reaction, on the one hand, and could point to the formation of extraframework mixed oxide species, on the other hand. The redistribution of Fe species is in line with the decrease of a Fe^{3+} Mössbauer component attributed to particles small enough to be accommodated in the micropores and a concomitant increase of the amount of Fe^{2+} sites. Moreover, a qualitative interpretation of nitrogen adsorption data indicates large changes in the structure of the micropores due to changes in the size of the occluded species. The increased Fe–Fe coordination number for this sample is attributable to further ordering and/or growth of the iron oxide aggregates on the external surface.

A steam treatment at 923 K results in a further redistribution of iron species. The fraction of large iron oxide aggregates slightly increases at the expense of the Fe^{3+} component with a QS of 1.53 $mm\,s^{-1}$, to be tentatively explained by a higher mobility of iron oxide species in the presence of water. This increased ordering of the majority of iron species is also reflected in the EXAFS fit parameters for Fe/ZSM-5(HTS) and a growing contribution of larger iron oxide particles (TEM). Concomitantly, an increase of Fe^{2+} species is observed by Mössbauer spectroscopy. Careful analysis suggests that the contribution of the Fe^{2+} component with QS = 3.42 $mm\,s^{-1}$ and IS = 1.82 $mm\,s^{-1}$ remains constant while a new Fe^{2+} species appears with QS = 3.55 $mm\,s^{-1}$ and IS = 1.40 $mm\,s^{-1}$. Finally, low-temperature nitrous oxide decomposition of a steamed HZSM-5 zeolite with a Fe content of 0.024 wt% shows that an amount of 0.0083 wt% iron is involved in the activation of nitrous oxide. This amount is considerably lower than in the sublimed samples, where active site concentrations in the range of 0.1–0.45 wt% were found. This excludes the possibility that the increase of the number of active sites in Fe/ZSM-5(HTC) and Fe/ZSM-5(HTS) compared to Fe/ZSM-5 only derives from dislodgement of the Fe contamination in the starting zeolite material. We take this observation as an indication that removal of Al from lattice positions may play a role in the formation of the active sites, a point to be further discussed in the companion paper [50].

4. Conclusions

Fe/ZSM-5, prepared by sublimation of $FeCl_3$ followed by washing and calcination, contains a large variety of Fe species. Iron oxide particles on the external zeolite surface are dominating (TEM, Mössbauer), while neutral iron oxide nanoparticles and charge-compensating iron complexes are located in the micropores (IR, Mössbauer). High-temperature calcination induces the growth and ordering of the iron oxide aggregates (TEM, Mössbauer, EXAFS, UV–vis) next to a protolysis reaction between occluded neutral iron oxide nanoparticles and Brønsted protons (IR). These effects are more pronounced in the case of steaming at 973 K, a treatment additionally leading to dealumination. Relatively low Fe–Fe coordination numbers were derived from Fe *K*-edge EXAFS measurements. This should be taken as an indication of the disordered nature of the abundantly present iron oxide aggregates rather than as evidence for the predominant presence of binuclear clusters. More importantly from a catalysis point of view, we conclude that high-temperature treatments lead to a larger number of sites able to decompose nitrous oxide at relatively low temperatures. The number of such active sites, however, is quite small and constitutes only a small fraction of the total iron content (3–12%). Moreover, the amount of active sites correlates to the amount of Fe^{2+} as probed by ^{57}Fe Mössbauer spectroscopy at 4.2 K. Tentatively, the observation that approximately one oxygen atom is deposited per two Fe^{2+} atoms agrees with the earlier proposed binuclear nature of the active sites.

Acknowledgments

The authors thank G.I. Panov and his colleagues (Boreskov Institute of Catalysis, Novosibirsk, Russia) for the low-temperature nitrous oxide decomposition measurements and useful discussion. Ms. M. Mittelmeijer of the University of Amsterdam is acknowledged for the nitrogen adsorption measurements. K.-J. Chao and her colleagues (Tsing Hua University, Hsinchu, Taiwan) are gratefully acknowledged for making available synchrotron beam time at the SRRC (Hsinchu, Taiwan). The Dutch National Research School Combination Catalysis is acknowledged for financial support.

References

[1] G. Centi, B. Wichterlova, A.T. Bell (Eds.), Catalysis by Unique Metal Ion Structures in Solid Matrices, in: NATO Science Series, Kluwer Academic, Dordrecht, 2001.
[2] A. Corma, J. Catal. 216 (2003) 298.
[3] G.I. Panov, CatTech 4 (2000) 18.
[4] A.K. Uriarte, M.A. Rodkin, M.J. Gross, A.S. Kharithonov, G.I. Panov, Stud. Surf. Sci. Catal. 110 (1997) 857.
[5] G. Centi, F. Vazzana, Catal. Today 53 (1999) 683.
[6] El-M. El Malki, R.A. van Santen, W.M.H. Sachtler, Micropor. Mesopor. Mater. 35–36 (2000) 235.
[7] El-M. El Malki, R.A. van Santen, W.M.H. Sachtler, J. Catal. 196 (2000) 212.
[8] J. Pérez-Ramírez, F. Kapteijn, G. Mul, X. Xu, J.A. Moulijn, Catal. Today 76 (2002) 55.
[9] Q. Zhu, B.L. Mojet, R.A.J. Janssen, E.J.M. Hensen, J. Van Grondelle, P.C.M.M. Magusin, R.A. van Santen, Catal. Lett. 81 (2002) 205.
[10] Q. Zhu, E.J.M. Hensen, B.L. Mojet, J.H.M.C. van Wolput, R.A. van Santen, Chem. Commun. (2002) 1232.
[11] R.Q. Long, R.T. Yang, J. Catal. 207 (2002) 224.
[12] X. Feng, W.K. Hall, Catal. Lett. 41 (1996) 45.
[13] X. Feng, W.K. Hall, J. Catal. 166 (1997) 368.
[14] L.J. Lobree, I.-C. Hwang, J.A. Reimer, A.T. Bell, Catal. Lett. 63 (1999) 233.
[15] H.-Y. Chen, T. Voskoboinikov, W.M.H. Sachtler, Catal. Today 54 (1999) 483.
[16] E. Suzuki, K. Nakashiro, Y. Ono, Chem. Lett. (1988) 953.
[17] R. Burch, C. Howitt, Appl. Catal. A 103 (1993) 135.
[18] V.L. Zholobenko, I.N. Senchenya, L.M. Kustov, V.B. Kazansky, Kinet. Catal. 32 (1991) 151.
[19] L.M. Kustov, A.L. Tarasov, V.I. Bogdan, A.A. Tyrlov, J.W. Fulmer, Catal. Today 61 (2000) 123.
[20] J.L. Motz, H. Heinrichen, W.F. Hölderich, J. Mol. Catal. 136 (1998) 175.
[21] A.S. Kharitonov, G.A. Sheveleva, G.I. Panov, V.I. Sobolev, Y.A. Paukshtis, V.N. Romannikov, Appl. Catal. A 98 (1993) 33.
[22] G.I. Panov, V.I. Sobolev, A.S. Kharitonov, J. Mol. Catal. 61 (1990) 85.
[23] G.I. Panov, G.A. Sheveleva, A.S. Kharitonov, V.N. Romannikov, L.A. Vostrikova, Appl. Catal. A 82 (1992) 31.
[24] P. Notté, Top. Catal. 13 (2000) 387.
[25] P. Kubánek, B. Wichterlová, Z. Sobalík, J. Catal. 211 (2002) 109.
[26] G. Berlier, A. Zecchina, G. Spoto, G. Ricchiardi, S. Bordiga, C. Lamberti, J. Catal. 215 (2003) 264.
[27] D. Meloni, R. Monaci, V. Solinas, G. Berlier, S. Bordiga, I. Rossetti, C. Oliva, L. Forni, J. Catal. 214 (2003) 169.
[28] P. Ratnasamy, R. Kumar, Catal. Today 9 (1991) 329.
[29] S.A. Axon, K.K. Fox, S.W. Carr, J. Klinowski, Chem. Phys. Lett. 189 (1992) 1.
[30] V.I. Sobolev, G.I. Panov, A.S. Kharitonov, V.N. Romannikov, A.M. Volodin, K.G. Ione, J. Catal. 139 (1993) 435.
[31] D.W. Lewis, R.A. Catlow, J. Sankar, S.W. Carr, J. Phys. Chem. 99 (1995) 2377.
[32] S. Bordiga, R. Buzzoni, F. Geobaldo, C. Lamberti, E. Giamello, A. Zecchina, G. Leofanti, G. Petrini, G. Tozzola, G. Vlaic, J. Catal. 158 (1996) 486.
[33] A. Ribera, I.W.C.E. Arends, S. de Vries, J. Pérez-Ramírez, R.A. Sheldon, J. Catal. 195 (2000) 287.
[34] G. Spoto, A. Zecchina, G. Berlier, S. Bordiga, M.G. Clerici, L. Basini, J. Mol. Catal. A 158 (2000) 107.
[35] G. Berlier, G. Spoto, S. Bordiga, G. Ricchiardi, P. Fisicaro, A. Zecchina, I. Rossetti, E. Selli, L. Forni, E. Giamello, C. Lamberti, J. Catal. 208 (2002) 64.
[36] A.M. Ferretti, C. Oliva, L. Forni, G. Berlier, A. Zecchina, C. Lamberti, J. Catal. 208 (2002) 83.
[37] L.V. Pirutko, V.S. Chernyavsky, A.K. Uriarte, G.I. Panov, Appl. Catal. A 227 (2002) 143.
[38] A. Dubkov, N.S. Ovanesyan, A.A. Shteinman, K.A. Dubkov, V.I. Sobolov, G.I. Panov, Kinet. Catal. 39 (1998) 792.
[39] H.-Y. Chen, W.M.H. Sachtler, Catal. Today 42 (1998) 73.
[40] R. Joyner, M. Stockenhuber, J. Phys. Chem. B 103 (1999) 5963.
[41] M. Kögel, R. Mönning, W. Schwieger, A. Tissler, T. Turek, J. Catal. 182 (1999) 470.
[42] P. Marturano, A. Kogelbauer, R. Prins, J. Catal. 190 (2000) 460.
[43] P. Marturano, L. Drozdová, A. Kogelbauer, R. Prins, J. Catal. 192 (2000) 236.
[44] P. Marturano, L. Drozdová, A. Kogelbauer, R. Prins, Stud. Surf. Sci. Catal. 135 (2001) 1627.

[45] A.A. Battiston, J.H. Bitter, D.C. Kongingsberger, Catal. Lett. 66 (2000) 75.
[46] F. Heinrich, C. Schmidt, E. Löffler, M. Menzel, W. Grünert, J. Catal. 212 (2002) 157.
[47] A.A. Battiston, J.H. Bitter, F.M.F. de Groot, A.R. Overweg, O. Stephan, J.A. van Bokhoven, P.J. Kooyman, C. van der Spek, G. Vankó, D.C. Koningsberger, J. Catal. 213 (2003) 251.
[48] A. Reitzmann, H. Friedrich, E. Klemm, M. Haefele, G. Emig, in: M. Rozwadoski (Ed.), Proc., Polish–German Zeolite Colloquium 3rd, Nicholas Copernicus Univ. Press, Torún, 1998, p. 239.
[49] T. Voskoboinikov, H-.Y. Chen, W.M.H. Sachtler, Appl. Catal. B 19 (1998) 279.
[50] Q. Zhu, R.M. van Teeffelen, R.A. van Santen, E.J.M. Hensen, J. Catal.
[51] H.-Y. Chen, W.M.H. Sachtler, Catal. Lett. 50 (1998) 125.
[52] M. Vaarkamp, J.C. Linders, D.C. Koningsberger, Phys. B (1995) 209.
[53] D.C. Koningsberger, B.L. Mojet, G.E. van Dorssen, D.E. Ramaker, Top. Catal. 10 (2000) 143.
[54] T.J.G. Kofke, R.J. Gorte, W.E. Fameth, J. Catal. 114 (1988) 34.
[55] K.A. Dubkov, V.I. Sobolev, G.I. Panov, Kinet. Katal. 39 (1998) 79.
[56] K.A. Dubkov, N.S. Ovanesyan, A.A. Shteinman, E.V. Starokon, G.I. Panov, J. Catal. 207 (2002) 341.
[57] G. Centi, F. Fazzini, J.L.G. Fierro, M. Lopèz Granados, R. Sanz, D. Serrano, in: B. Delmon, et al. (Eds.), Preparation of Catalysts VII, 1998, p. 577.
[58] P.A. Webb, C. Orr, in: Analytical Methods in Fine Particles Technology, Micromeritics Instrument Corporation, Norcross, USA, 1997, pp. 59–73.
[59] G. Calas, J. Petiau, J. Solid State Commun. 48 (1983) 625.
[60] J. Pérez-Ramírez, G. Mul, F. Kapteijn, J.A. Moulijn, A.R. Overweg, A. Doménech, A. Ribera, I.W.C.E. Arends, J. Catal. 207 (2002) 113.
[61] T.V. Voskoboinikov, H.-Y. Chen, W.M.H. Sachtler, J. Mol. Catal. A 155 (2000) 155.
[62] K. Lázar, A.N. Kotasthane, R. Fejes, Catal. Lett. 57 (1999) 171.
[63] M. Mauvezin, G. Delahay, B. Coq, S. Kieger, J.C. Jumas, J. Oliver-Fourcade, J. Phys. Chem. B 105 (2001) 928.
[64] G.I. Panov, A.K. Uriarte, M.A. Rodkin, V.I. Sobolev, Catal. Today 41 (1998) 365.
[65] G.I. Panov, V.I. Sobolev, K.A. Dubkov, V.N. Parmon, N.S. Ovanesyan, A.E. Shilov, A.A. Shteinman, React. Kinet. Catal. Lett. 61 (1997) 251.
[66] G.I. Panov, V.I. Sobolev, K.A. Dubkov, A.S. Kharitonov, Stud. Surf. Sci. Catal. 101 (1996) 493.
[67] T. Shido, R. Prins, J. Phys. Chem. B 102 (1998) 8426.